



Final Draft of the original manuscript

Aschauer, E.; Bartosik, M.; Bolvardi, H.; Arndt, M.; Polcik, P.; Davydok, A.; Krywka, C.; Riedl, H.; Mayrhofer, P.H.:

Strain and stress analyses on thermally annealed Ti-Al-N/Mo-Si-B multilayer coatings by synchrotron X-ray diffraction.

In: Surface and Coatings Technology. Vol. 361 (2019) 364 – 370.

First published online by Elsevier: 23.01.2019

<https://dx.doi.org/10.1016/j.surfcoat.2019.01.075>

Strain and stress analyses on thermally annealed Ti-Al-N/Mo-Si-B multilayer coatings by synchrotron X-ray diffraction

E. Aschauer¹, M. Bartosik², H. Bolvardi³, M. Arndt³, P. Polcik⁴, A. Davydok⁵, C. Krywka⁵,
H. Riedl^{1,2}, and P.H. Mayrhofer^{1,2}

¹ Christian Doppler Laboratory for Application Oriented Coating Development, TU Wien, Austria

² Institute of Materials Science and Technology, TU Wien, Austria

³ Oerlikon Balzers, Oerlikon Surface Solutions AG, Liechtenstein

⁴ Plansee Composite Materials GmbH, Germany

⁵ Institute for Materials Research, Helmholtz-Zentrum Geesthacht, Germany

Abstract

In order to analyse the main failure mechanism of multilayered coating material in oxidative environments, we separately investigated the cross-sectional strain/stress evolution induced by thermal loads and oxidation for the Ti-Al-N/Mo-Si-B model system. The bilayer period (Λ) of the crystalline Ti-Al-N/amorphous Mo-Si-B layers was varied between 26, 130, 240, and 1085 nm. The stress state was characterised by synchrotron X-ray nano-diffraction, using monochromatic X-ray radiation with a beam size of around 200 x 300 nm². This allows for analysing the spatially resolved strain/stress evolution of the as-deposited state as well as after thermally treated coatings – either 1 h annealed in vacuum or ambient air at 900 °C. For small bilayer periods, the alteration of face centred cubic Ti-Al-N by amorphous Mo-Si-B layers effectively reduces the as-deposited compressive strain profile along the growth direction. Furthermore, for $\Lambda \leq 130$ nm, the decomposition of Ti-Al-N to form hexagonal structured AlN as well as the crystallisation of the Mo-rich layers towards the intermetallics Mo₅SiB₂ and Mo₅Si₃ is significantly delayed. After oxidation, the oxide scale grows in the low-compressive stress regime, while the intact multilayer shows similar microstructural changes as the vacuum annealed coatings.

Keywords: Mo-Si-B; Multilayer; Nanobeam; Residual strain; Spinodal decomposition; Oxidation resistance

1 Introduction

Physical vapour deposited (PVD) $Ti_{1-x}Al_xN$ is one of the most prominent and versatile protective coatings used in various industrial applications, due to the outstanding thermomechanical properties [1,2].

Face centred cubic (fcc) solid solution $Ti_{1-x}Al_xN$ is a metastable or even instable phase (depending on the Al content [3]), which upon thermal loading decomposes into the constituting thermodynamically stable boundary phases fcc-TiN and hexagonal closed packed AlN (having a wurtzite-ZnS structure, therefore abbreviated here with w). Typically this decomposition starts at around 900 °C via the spinodal decomposition induced formation of fcc-AlN rich domains, leading to age hardening effects. The formation of the thermodynamically stable w-AlN phase typically starts at around 1000 °C and is accompanied by a decrease in mechanical properties, especially if its fraction rapidly increases (because w-AlN has lower mechanical strength than fcc-AlN or fcc-TiN, represented also by its significantly larger bond lengths. The significantly larger specific volume of w-AlN as compared to fcc-AlN ($\Delta V \sim 26\%$, [4]) generates an increase in compressive stresses [5,6], which can lead to cracks and delamination effects, but can also be used beneficially if its phase fraction and transformation sequence is controlled [7,8].

However, in various applications, $Ti_{1-x}Al_xN$ is not only loaded by thermal stresses but also by oxidising atmosphere, leading to the formation of Al_2O_3 and TiO_2 based oxides. These oxides, especially TiO_2 , often lead to the formation of surface induced crack formation [9] due to their different specific volume, thermal expansion and elastic constants [10]. These will lead to different stress levels within the oxide (and consequently the coating on which the oxide scale is formed) where for TiO_2 , the possible phase transformation from anatase to rutile, can lead to additional stress sources [11]. Therefore, the stress development due to microstructural changes within the coating itself but also due to the oxidation process and ongoing changes in the oxide is of utmost importance. These superimposed mechanisms are often difficult to separate [12]. But especially for such quests, the cross-sectional investigation of (oxidised) coatings by position-resolved synchrotron X-ray nano-diffraction is helpful [13]. This technique is also ideal when analysing the microstructural changes and strain changes along the growth direction of coatings, especially when having a gradient or multilayer coating [14–17]. Within our previous studies [18–20], we showed that a multilayer arrangement of fcc structured $Ti_{1-x}Al_xN$ and amorphous-like Mo-Si-B layers can be highly beneficial for high thermal stability of strength and oxidation resistance. The periodically interrupted columnar growth (especially when the combined layers do not grow coherently, or when the coherency strains are so high that repeated nucleation is promoted) is beneficial for mechanical strength as well as oxidation resistance, because the weak bonds between columns and their generally rather open

microstructure reduces strength and promotes diffusion. Hence, especially oxygen can rapidly, via these diffusion pathways, enter the coating [20].

70 But also phase transformations, especially within $Ti_{1-x}Al_xN$ layers, are hugely influenced by an altered arrangement of layers. For example, the formation of $w-AlN$ is significantly retarded by an altered arrangement with TiN [21]. Many stress related studies analysing multilayered or gradient thin films after thermal exposure have been focused on treatments in either inert or oxidising atmosphere [14,22]. However, little information are available were the impact of both (inert and oxidising atmospheres) are discussed for one material system.

Therefore, we investigated the strain and stress evolution of our recently developed $Ti_{1-x}Al_xN/Mo-Si-B$ multilayers – having bilayer periods of 1085 nm (1000 nm $Ti-Al-N$ and 85 nm $Mo-Si-B$), 240 nm (200 nm $Ti-Al-N$ and 40 nm $Mo-Si-B$), 130 nm (100 nm $Ti-Al-N$ and 30 nm $Mo-Si-B$), and 26 nm (21 nm $Ti-Al-N$ and 5 nm $Mo-Si-B$) – by cross sectional synchrotron X-ray nano-diffraction after thermal exposure in vacuum and oxidising atmosphere, respectively.

2 Experimental

80 All $Ti-Al-N/Mo-Si-B$ multilayer coatings were deposited onto mono-crystalline (1102) oriented sapphire, and (100) oriented silicon substrates, as well as low alloyed steel foil, using an industrial scale Oerlikon Balzers INNOVA deposition system, equipped with powder metallurgically manufactured $Ti_{0.5}Al_{0.5}$ and $Mo_{0.5}Si_{0.3}B_{0.2}$ targets (Plansee Composite Materials GmbH). The multilayer architecture is supported by alternatingly covering the constantly operating $Ti_{0.5}Al_{0.5}$ cathodes or $Mo_{0.5}Si_{0.3}B_{0.2}$ targets with shutters. For the $Ti_{1-x}Al_xN$ layers, deposited by arc evaporation, a nitrogen gas flow of 1000 sccm (purity 5.0), a bias voltage of -65 V, and a cathode current of 150 A was used. The $Mo-Si-B$ layers, synthesised by DC magnetron sputtering, were grown with a power density of $\sim 13.5 W/cm^2$, a bias potential of -40 V, and an argon flow of 500 sccm (purity 5.0). To guarantee for a sufficient gas exchange between the individual layers, the shutters in front of the $Mo_{0.5}Si_{0.3}B_{0.2}$ targets are opened 5 s after the shutters in front of the $Ti_{0.5}Al_{0.5}$ cathodes were closed, and vice versa. The substrate temperature during the deposition process was constantly held at $\sim 500^\circ C$ and a two-fold rotating substrate carousel (ca. 1.6 revolutions/min) was used. Prior to the deposition, all substrates were ultrasonically cleaned in acetone and ethanol for 5 min each, as well as argon ion etched within the deposition chamber, using the Oerlikon Balzers central beam etching technology.

90

Tab. 1: Architecture of the investigated $Ti_{1-x}Al_xN/Mo-Si-B$ multilayer coatings, with Λ for the bilayer period, consisting of λ_1 (layer thickness of $Ti_{1-x}Al_xN$) and λ_2 (layer thickness of $Mo-Si-B$) and n_i for the total number of interfaces.

Λ [nm]	Coating thickness [nm]	λ_1 ($Ti_{1-x}Al_xN$) [nm]	λ_2 ($Mo-Si-B$) [nm]	Number of interfaces n_i	λ_1/λ_2
1085	2170	1000	85	3	12:1
240	1900	200	40	15	5:1
130	2100	100	30	31	3.3:1
26	3120	21	5	239	4:1

To investigate the influence of interfaces between the crystalline $Ti_{1-x}Al_xN$ and the amorphous $Mo-Si-B$ layers, we deposited 4 different coating architectures with decreasing bilayer periods Λ , consisting of λ_1 (layer thickness of $Ti_{1-x}Al_xN$) and λ_2 (layer thickness of $Mo-Si-B$), and increasing number of interfaces n_i , see Tab. 1. This was realised by altering the deposition times of the respective cathodes/targets during the synthesis.

For comparison reasons, also a monolithically grown $Ti_{1-x}Al_xN$ film was arc evaporated, using 1000 sccm N_2 gas flow (purity 5.0), a bias potential of -65 V, and a cathode current of 150 A.

To get a firm crystallographic analysis of the coatings in the as-deposited state, we performed powder X-ray diffraction measurements, using an Empyrean Panalytical diffractometer in Bragg-Brentano geometry (equipped with a $Cu_{K\alpha}$ -radiation source with $\lambda = 1.5418 \text{ \AA}$). The powdered thin film material was obtained by dissolving the coated steel foil in diluted HCl and grinding the residual coating material in a ceramic mortar.

The annealing experiments were carried out on coated sapphire platelets in ambient air (Nabertherm N11/HR furnace) and vacuum (Centorr LF22-2000, base pressure $< 3 \cdot 10^{-5}$ mbar) at 900 °C for 1 h, utilising a heating rate of 20 K/min. Both systems were passively cooled down to room temperature, obtaining cooling rates of approximately 50 K/min until 500 °C.

For cross-sectional bright-field transmission electron microscopy (BF-TEM), high-resolution TEM (HR-TEM), and selected area electron diffraction (SAED) investigations, two coated silicon substrates were glued coating-to-coating (and mechanically polished down to $< 30 \mu m$). In a further step, they were ion beam milled to electron transparency, using a Gatan PIPS machine. The TEM investigations were carried out on a 200 kV FEI TECNAI F20 S-TWIN transmission electron microscope. For the cross-sectional scanning electron microscopy (SEM) investigations, a FEI Quanta 200 FEG was utilised, applying an accelerating voltage of 10 kV as well as a spot size of 3.0.

130 The X-ray nano-beam diffraction experiments were carried out on coated sapphire substrates in the as-deposited as well as annealed states (vacuum and oxidising atmosphere). The substrates were mechanically polished down to X-ray transmission thickness of about 50 μm , using a grain size of 1 μm during the final polishing step. The measurements of the multilayer coatings were carried out at the nanofocus endstation of the beamline P03 of the light source PETRA III at the “Deutsche Elektronen Synchrotron” (DESY) in Hamburg, Germany [23]. The Debye-Scherrer rings were recorded in transmission geometry (see Fig. 1) by following a nano-diffraction transmission approach [13,24], using monochromatic synchrotron X-ray radiation (energy ~ 15 keV, wavelength in the range of 0.82 \AA), focused with Kirkpatrick-Baez mirrors and a cross-section of 250 nm, see Fig. 1. During the measurements, the sample was moved in 100 nm steps in z-direction to obtain a cross-sectional analysis. The diffraction patterns were recorded by a charge-coupled device detector (CCD), placed around 19 cm behind the sample (calibrated by using standardised powdered LaB_6), with an acquisition time of ca. 10 s per frame. Using this setup, we were able to collect diffraction patterns with Bragg angles of up to around 32° (which corresponds to approximately 60° when using $\text{Cu}_{K\alpha}$ radiation). By following this approach, we were able to assign the collected Debye-Scherrer cones to the

140 corresponding coating depth position.

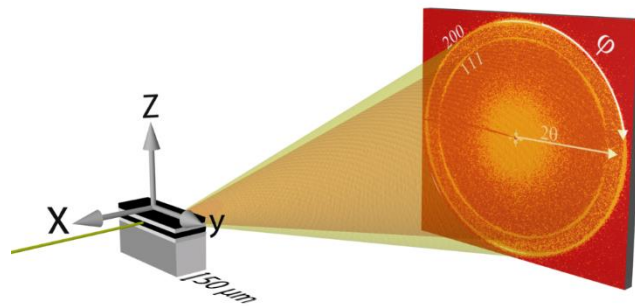


Fig. 1: Schematic overview of the experimental setup of the nano-diffraction experiments, carried out in transmission geometry. The film is aligned parallel to the incoming beam and scanned in 100 nm steps in z-axis direction. The CCD detector collects diffractions peaks at Bragg angles of up to $\sim 32^\circ$.

After processing the obtained two-dimensional diffraction data using the program package Fit2D [25], the residual X-ray in-plane strain ε^{hkl} was calculated after the $\sin^2\phi$ -method, where the elliptical distortion of the obtained Debye-Scherrer rings of the respective Bragg reflex at 2θ is determined for azimuthal angle ϕ (see Eq. 1) [26].

$$\varepsilon^{hkl}(z) \approx \frac{1}{d_{hkl}} \frac{\partial a(\phi, z)}{\partial \sin^2 \phi} \quad (1)$$

Because of the absence of distinct Bragg reflexes of the Mo-Si-B layers due to its amorphous nature in the as-deposited state [18], we evaluated the residual in-plane strain within the coating by analysing the 200 reflex of $\text{Ti}_{1-x}\text{Al}_x\text{N}$ and the 100 and 012 reflex for rutile- TiO_2 and corundum- Al_2O_3 , respectively.

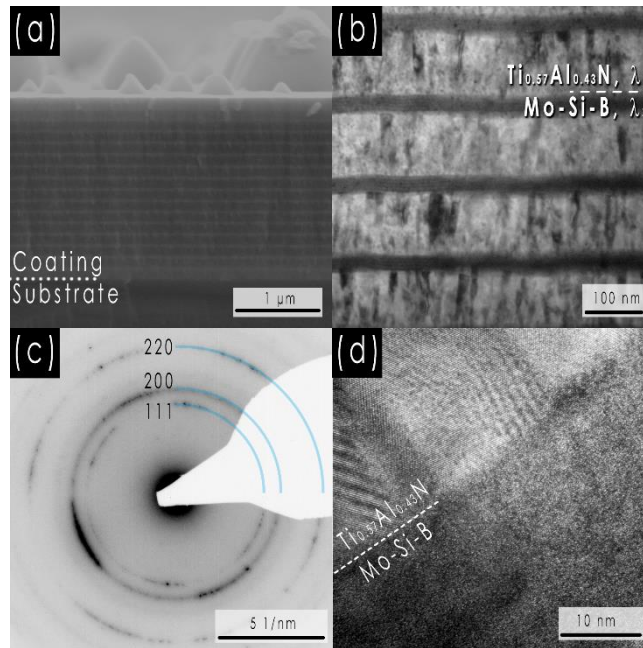
3 Results and Discussion

3.1 Structure and morphology

The chemistry of the coatings was determined by analysing the homogeneously grown counterparts by time of flight elastic recoil detection analysis (TOF-ERDA) of Mo-Si-B, corresponding to $\text{Mo}_{0.58}\text{Si}_{0.28}\text{B}_{0.14}$ (for further details see reference [19,27]), as well as by energy dispersive X-Ray spectroscopy (EDX) of $\text{Ti}_{1-x}\text{Al}_x\text{N}$, leading to a nitrogen normalised composition of $\text{Ti}_{0.57}\text{Al}_{0.43}\text{N}$ [19].

Figure 2 shows representative cross-sectional SEM (a), BF-TEM (b), SAED pattern (c) and HR-TEM (d) micrographs of the multilayer with a bilayer period of $\Lambda = 130$ nm [$\lambda_1=100$ nm ($\text{Ti}_{0.57}\text{Al}_{0.43}\text{N}$) and $\lambda_2 = 30$ nm (Mo-Si-B)]. The coating show a dense, homogeneous fracture cross-section, exhibiting a uniform bilayer period over the entire coating thickness, Fig. 2a. The BF-TEM image (Fig. 2b) reveals a V-shaped columnar grain morphology within the $\text{Ti}_{0.57}\text{Al}_{0.43}\text{N}$ layers [28] (typical for PVD deposited thin films), which are repeatedly interrupted by the alternating $\text{Mo}_{0.58}\text{Si}_{0.28}\text{B}_{0.14}$ layers.

The $\text{Ti}_{0.57}\text{Al}_{0.43}\text{N}$ layers are forced to renucleate after each $\text{Mo}_{0.58}\text{Si}_{0.28}\text{B}_{0.14}$ layer, which prevents the formation of continuous columns (ranging from the substrate to the top of the coating) and consequently influences the grain size significantly. The full width at half maximum (FWHM) value of the 200 reflex, obtained from the XRD measurements of powdered coating material, which inversely correlates with the grain size, increases from 0.640 to 0.868 to 1.008 to 1.388° with decreasing bilayer period from $\Lambda = 1085, 240, 130,$ and 26 nm. The homogeneously grown $\text{Ti}_{0.57}\text{Al}_{0.43}\text{N}$ exhibits a FWHM value of the 200 reflex of 0.566°. The corresponding SAED pattern (Fig. 2c), obtained with an aperture (size of 750 nm) positioned over multiple bilayers, reveals fcc crystal structures of $\text{Ti}_{0.57}\text{Al}_{0.43}\text{N}$ as well as the amorphous character of the $\text{Mo}_{0.58}\text{Si}_{0.28}\text{B}_{0.14}$ layers.



180 *Fig.2: Cross-sectional SEM (a), TEM (b) and HR-TEM (d) investigations as well as SAED pattern of the coating (c) with 16 bilayers (=31 interfaces) and a bilayer period of $\Lambda=130$ nm, consisting of $\lambda_1=100$ nm ($Ti_{0.57}Al_{0.43}N$) and $\lambda_2 = 30$ nm ($Mo-Si-B$).*

This is also supported by the HR-TEM (Fig. 2d), showing a highly crystalline $Ti_{0.57}Al_{0.43}N$ growing on a featureless, amorphous $Mo_{0.58}Si_{0.28}B_{0.14}$ layer, having no near-range order or any crystalline nano-clusters within the analysed volume.

For more details on the chemical and structural properties of the coating system, please see our previous studies [18,20].

3.2 Nano-beam diffraction experiments

190 Figures 3a to c give the depth resolved 2θ nano-diffraction intensity plots (obtained by integration of the measured Debye-Scherrer rings) of monolithically grown $Ti_{0.57}Al_{0.43}N$ as well as multilayers with bilayer periods of 1085 and 130 nm in their as-deposited state. Please note that small misalignments of the sample, e.g., when the sample is tilted around the y -axis (Fig. 1), can lead to a significant reduction in vertical resolution. To compensate possible deviations of the coating thickness and the number of collected frames, all 2θ vs. nano-beam diffraction intensity plots were normalised to the coating thickness obtained by SEM.

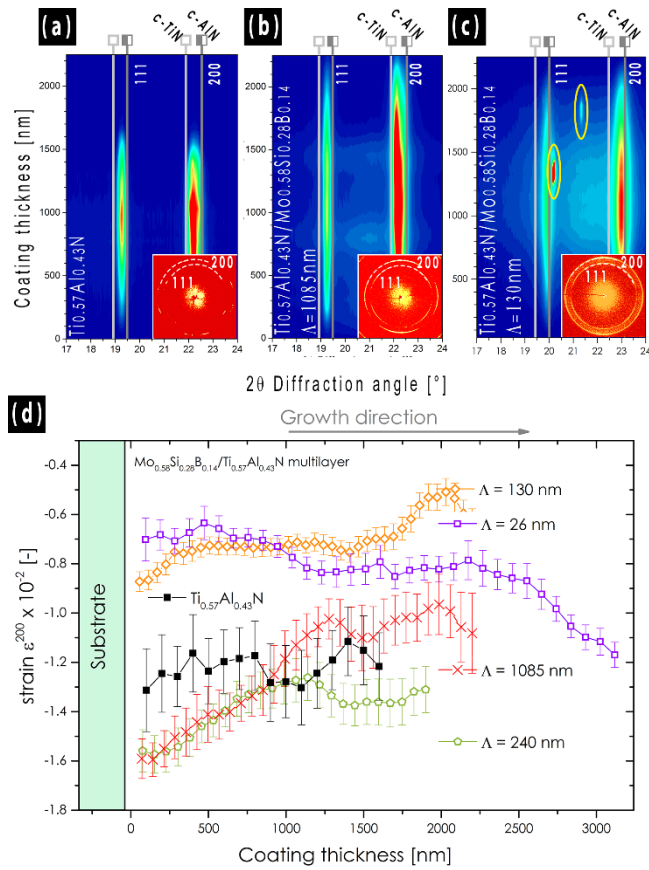


Fig. 3: As-deposited 2θ vs. nano-beam diffraction intensity plots of homogeneously grown $Ti_{0.57}Al_{0.43}N$ and of selected bilayer periods ($\Lambda=1085$ nm and $\Lambda=130$ nm) in dependency of the coating thickness with inserted, selected Debye-Scherrer rings (a to c) as well as the corresponding strain values (d). All coatings are composed of a fcc $Ti_{0.57}Al_{0.43}N$ matrix layer as well as an (X-ray)- amorphous $Mo_{0.58}Si_{0.28}B_{0.14}$ interlayer, showing decreasing strain values with decreasing bilayer thickness.

Furthermore, it is worth mentioning, that homogeneously grown $Ti_{0.57}Al_{0.43}N$ as well as the multilayers with a bilayer period of 1085 and 240 nm were recorded with a smaller wavelength ($\lambda = 0.80533$ Å compared to $\lambda = 0.82650$ Å), leading to slightly shifted 2θ values.

The nano-beam diffraction intensity plots confirm the results of the SAED studies (as presented in Fig. 2c) and again highlight the single phased fcc nature of $Ti_{0.57}Al_{0.43}N$ as well as the amorphous character of the $Mo_{0.58}Si_{0.28}B_{0.14}$ layers. These $Mo_{0.58}Si_{0.28}B_{0.14}$ layers yield an increased background between the fcc $Ti_{0.57}Al_{0.43}N$ 111 and 200 reflexes, which increases with decreasing bilayer period. As marked in Fig. 3c, some of the coatings show additional diffraction reflexes. By using SAED and EDX within TEM, we could relate them to intermetallic, Ti-Al rich phases, stemming from macroparticles (often referred to as droplets) from the cathode surface [29,30].

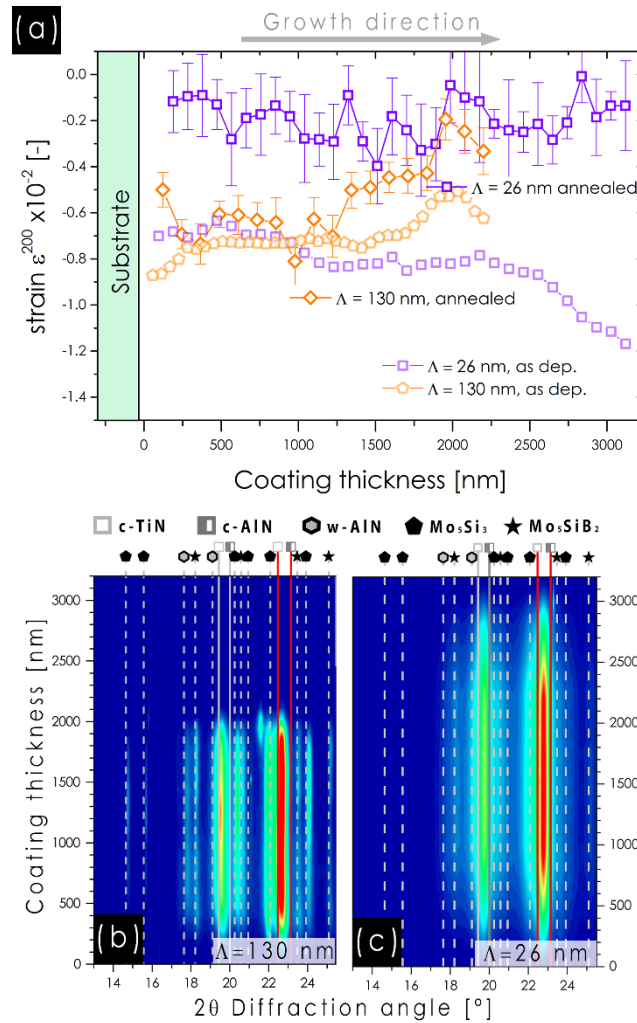
The as-deposited residual in-plane strain $\epsilon_{Ti_{0.57}Al_{0.43}N}^{200}$ across the coating thickness is presented in Fig. 3d. All coatings are in the compressive strain regime, due to the arc evaporation of $Ti_{0.57}Al_{0.43}N$ and the differential thermal expansion coefficient between the sapphire substrate ($\alpha_{Sapphire} = 8.6 \cdot 10^{-6} K^{-1}$ [31]) and the main constituent of the coating ($\alpha_{Ti_{0.50}Al_{0.50}N} = 7.5 \cdot 10^{-6} K^{-1}$ [32,33]) [34].

220 For homogeneously grown $Ti_{0.57}Al_{0.43}N$ as well as for the coatings with the lowest number of interfaces ($\Lambda = 1085$ and 240 nm), we found the highest compressive strain values in the range of $\epsilon^{200} \sim -1.4$ %, which are directly at the interface to the substrate. These coatings also show the largest error bars for the strain values, most likely due to the broader variation in grain size within the $Ti_{0.57}Al_{0.43}N$ layer due to their pronounced competitive growth processes. The coarse-grained coating morphology of the monolithic film leads to a spotty diffraction pattern, which makes the strain evaluation more challenging and explains the relatively large error bars of the corresponding black curve in Fig. 1. For smaller bilayer periods, the average grain size is much smaller, as indicated by more continuous Debye-Scherrer rings (insets of Fig. 3a, b, and c).

230 For multilayers with $\Lambda = 130$ and 26 nm, the in-plane strain ϵ^{200} close to the substrate is -0.9 % and -0.7 %, respectively, and thus significantly smaller as compared to homogeneously grown $Ti_{0.57}Al_{0.43}N$ (and multilayers with larger bilayer periods). Similar relationships between the bilayer period and the residual in-plane strain were also observed by Ljungcrantz et al. [35] within TiN/NbN multilayer coatings, which also showed reduced strain values as compared to the homogeneously grown material systems. This relation is based on the strain generation within the growing $Ti_{0.57}Al_{0.43}N$ crystals, which is repeatedly interfered by the growth of the amorphous-like Mo-Si-B layers.

240 Interestingly, the strain profile (along the coating thickness in growth direction) also significantly changes with decreasing bilayer period. For larger bilayer periods, the strains initially relax (similar to homogeneously grown $Ti_{0.57}Al_{0.43}N$ to $\epsilon^{200} \sim -1.0$ % at 1500 nm ($\Lambda = 1085$ nm), $\epsilon^{200} \sim -1.3$ % at 1000 nm ($\Lambda = 240$ nm), and $\epsilon^{200} \sim -0.7$ % at 500 nm ($\Lambda = 130$ nm). The multilayer with the smallest bilayer period ($\Lambda = 26$ nm) even shows increasing ϵ^{200} values with increasing coating thickness, from ~ -0.7 % at 500 nm to ~ -1.2 % at 3500 nm, see Fig. 3d. These are important results, as they show that with decreasing bilayer period the loading at the interface to the substrate significantly decreases. When using the elastic constants of $Ti_{0.50}Al_{0.50}N$ in the $\langle 200 \rangle$ direction [34], the loading at the interface decreases from -5.40 GPa ($\epsilon^{200} \sim -1.6$ % for $\Lambda = 1085$ nm) to -2.75 GPa ($\epsilon^{200} \sim -0.7$ % for $\Lambda = 26$ nm).

At a coating thickness of 1800 nm, the multilayer with a bilayer period of $\Lambda = 130$ nm exhibits a pronounced strain-peak, suggesting a localised decreased strain level, which could be caused by incorporated macro-particles (as mentioned before). This is also indicated by the additional diffraction spots at this coating thickness, highlighted in Fig. 3c.



250 Fig. 4: Strain evolution of vacuum annealed (vivid coloured) and as-deposited (pale coloured) $Ti_{0.57}Al_{0.43}N/Mo_{0.58}Si_{0.28}B_{0.14}$ multilayer coatings with a bilayer period of $\Lambda=130$ nm and $\Lambda=26$ nm (a) and the corresponding nano-beam diffraction intensity plots, showing the phase evolution for $\Lambda=130$ nm (b) and $\Lambda=26$ nm (c). The red coloured phase lines indicate the peaks used for the calculation of the residual strains. Please note that due to severe delamination during annealing, there are no data available for larger bilayer periods as well as for homogeneously grown $Ti_{0.57}Al_{0.43}N$.

The thermally induced and oxidation induced changes in the stress/strain state are investigated by studying vacuum and ambient air annealed (at 900 °C for 60 min) samples. During vacuum annealing at 900 °C, the homogeneously grown $Ti_{0.57}Al_{0.43}N$ coating and the $Ti_{0.57}Al_{0.43}N/Mo_{0.58}Si_{0.28}B_{0.14}$ multilayers with a bilayer period of $\Lambda = 240$ and 1085 nm experienced severe delamination from their sapphire substrate. Therefore, there are no strain data after annealing from these samples.

260 The strain state of the multilayer with $\Lambda = 130$ nm is almost unchanged as compared to the as-deposited state (Fig. 4a). However, the corresponding 2θ vs. nano-beam diffraction intensity plot (Fig. 4b) indicates a decomposition of fcc- $Ti_{0.57}Al_{0.43}N$ towards fcc-TiN and w-AlN, by the pronounced

270 shift of the fcc-Ti-Al-N 200 peak towards fcc-TiN and the formation of w-AlN (see e.g. the XRD peak at $2\theta=17.7^\circ$) [36]. Simultaneously, the initially amorphous $\text{Mo}_{0.58}\text{Si}_{0.28}\text{B}_{0.14}$ layers phase-transformed into Mo-based intermetallic phases $T_1\text{-Mo}_5\text{Si}_3$ (A15, cP8, Cr_3Si -prototype, e.g. $2\theta = 14.7^\circ$) and $T_2\text{-Mo}_5\text{SiB}_2$ (D8_I, tI32, Cr_5B_3 -prototype, e.g. $2\theta = 18.1^\circ$), in agreement with our earlier reports [18]. In contrast, the multilayer with the smallest bilayer period $\Lambda = 26$ nm exhibits a distinct decreased residual in-plane strain (Fig. 4a), as compared to the as-deposited state. Furthermore, the decomposition of fcc- $\text{Ti}_{0.57}\text{Al}_{0.43}\text{N}$ is less pronounced or progressed as compared to the coating with a bilayer period of $\Lambda = 130$ nm (indicated by the smaller peak shift of the Ti-Al-N 111 and 200 peaks), and the mentioned Mo-rich intermetallic phases T_1 and T_2 are significantly less pronounced (please compare Fig. 4b and c). A delayed decomposition of $\text{Ti}_{1-x}\text{Al}_x\text{N}$ when present in a multilayer system is also reported by Fei Wang et al. [21] for $\text{Ti}_{1-x}\text{Al}_x\text{N}/\text{TiN}$.

280 As the formation of w-AlN (upon decomposition of fcc- $\text{Ti}_{0.57}\text{Al}_{0.43}\text{N}$) is connected with a huge increase in volume (from 16.80 \AA^3 for fcc-AlN to 21.3 \AA^3 for w-AlN [4], any variation of the material that effectively hinders such a volume increase (like in a multilayer arrangement where rather thin $\text{Ti}_{1-x}\text{Al}_x\text{N}$ layers are encapsulated between other layers) will postpone the formation of w-AlN, as also reported by Fei Wang et al. [21].

In general, the $\text{Ti}_{0.57}\text{Al}_{0.43}\text{N}/\text{Mo}_{0.58}\text{Si}_{0.28}\text{B}_{0.14}$ multilayer will experience at least two superimposing mechanisms. One, which increases the strain due to the decomposition of fcc- $\text{Ti}_{1-x}\text{Al}_x\text{N}$ (to finally generate the spacious w-AlN) and the phase transformation of the initially amorphous $\text{Mo}_{0.58}\text{Si}_{0.28}\text{B}_{0.14}$, and one which releases strains due to recovery effects (where defects arrange in lower energy sites). For large bilayer periods ($\Lambda = 1085$ and 240 nm), the $\text{Ti}_{1-x}\text{Al}_x\text{N}$ decomposition-induced generation of compressive strains cannot be accommodated fast enough by recovery effects, leading to delamination effects. For smaller bilayer periods ($\Lambda = 130$ and 26 nm), the formation of the spacious w-AlN is effectively retarded, leading to a constant or decreasing residual strain level due to ongoing recovery effects.

290 Corresponding to the vacuum annealing experiments, we also observe delamination of the monolithically grown $\text{Ti}_{0.57}\text{Al}_{0.43}\text{N}$ coatings as well as $\text{Ti}_{0.57}\text{Al}_{0.43}\text{N}/\text{Mo}_{0.58}\text{Si}_{0.28}\text{B}_{0.14}$ multilayers with large bilayer periods ($\Lambda = 1085$ and 240 nm) during oxidation at ambient air at 900°C for one hour. The multilayers with smaller bilayer periods ($\Lambda = 130$ and 26 nm) however can (in addition to the vacuum annealing) withstand such a thermal treatment.

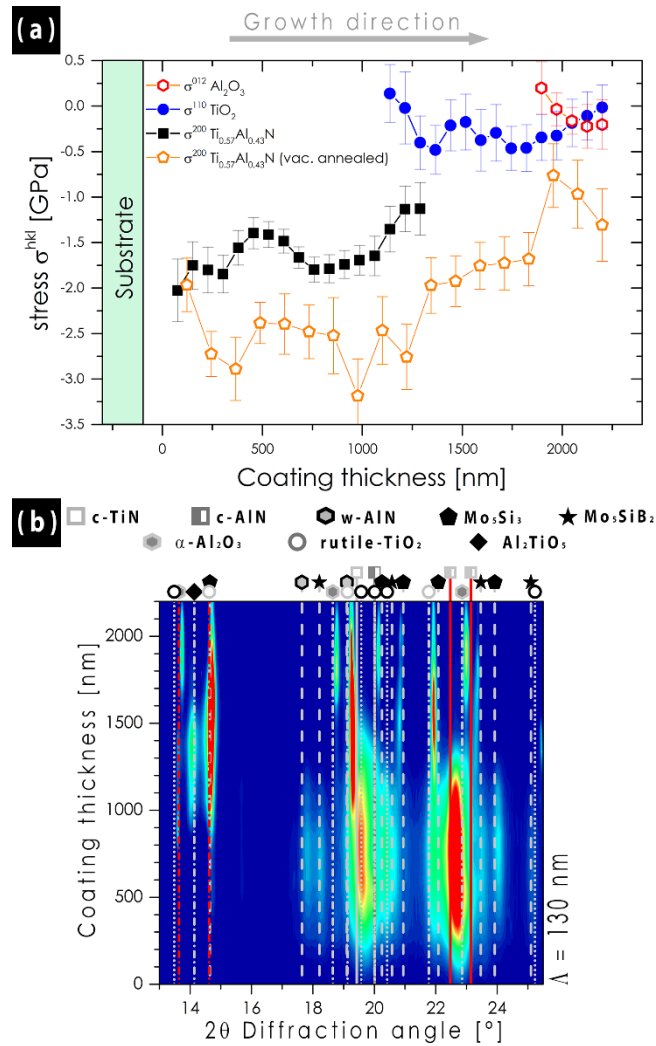


Fig. 5: Stress evolution of oxidised $\text{Ti}_{0.57}\text{Al}_{0.43}\text{N}/\text{Mo}_{0.58}\text{Si}_{0.28}\text{B}_{0.14}$ multilayer coatings with a bilayer period of $\Lambda=130$ nm (a) and the corresponding 2θ vs. nano-beam diffraction intensity plots (b). The red coloured phase lines indicate the peaks used for the calculation of the residual stress. In contrast to the as-deposited or vacuum annealed coatings, we transferred the strain data to stress values to ensure a comparability of the different crystalline phases. Please note that due to severe delamination and oxidation during annealing, there are no data available for larger bilayer periods as well as for homogeneously grown $\text{Ti}_{0.57}\text{Al}_{0.43}\text{N}$.

300

Due to the significantly different phases present after oxidation (remaining nitrides and forming oxides), and their significantly different elastic constants, we calculated the corresponding stresses from the measured strains, to compare them in an overview graph, Fig. 5a. There, the results for the major crystalline phases, $\text{Ti}_{0.57}\text{Al}_{0.43}\text{N}$, rutile $r\text{-TiO}_2$, and corundum $\alpha\text{-Al}_2\text{O}_3$ are presented using elastic constants of $\text{Ti}_{0.50}\text{Al}_{0.50}\text{N}$ in the [200] direction [34], $r\text{-TiO}_2$ in the [110] direction [35], and $\alpha\text{-Al}_2\text{O}_3$ in the [012] direction [36], respectively.

310

Figure 5a shows the stress evolution over the coating thickness of these phases for the multilayer with $\Lambda = 130$ nm. The results for the multilayer with $\Lambda = 26$ nm are very similar to these, but due to clarity not added. As compared to the vacuum annealed state, the compressive stresses are shifted to smaller values, however, the stress directly at the substrate/coating interface is for both heat treatments around ~ -2.0 GPa. Both multilayers show moderate compressive stresses for $\text{Ti}_{1-x}\text{Al}_x\text{N}$, and their oxide scale is in the low compressive or stress-free regime. One reason for that is the increasing volume of the participating unit cells, when referring the respective unit cell volumes to the number of reacted atoms. For the present oxidation of $\text{Ti}_{0.57}\text{Al}_{0.43}\text{N}$ to the oxide phases $r\text{-TiO}_2$ and $\alpha\text{-Al}_2\text{O}_3$, especially the $r\text{-TiO}_2$ is significantly larger than the corresponding nitride, $V_{\text{TiN}} \sim 19 \text{ \AA}^3/\text{Ti}$ and $V_{\text{TiO}_2} \sim 31 \text{ \AA}^3/\text{Ti}$, whereas $\alpha\text{-Al}_2\text{O}_3$ has nearly the same volume as fcc-AlN, $V_{\text{AlN}} \sim 17 \text{ \AA}^3/\text{Al}$ and $V_{\text{Al}_2\text{O}_3} \sim 21 \text{ \AA}^3/\text{Al}$. This would result in a modified Pilling-Bedworth-ratio of 1.64 for TiO_2 on fcc-TiN and 1.27 for Al_2O_3 on fcc-AlN (0.99 on w-AlN). In average for $\text{Ti}_{0.50}\text{Al}_{0.50}\text{N}$, the Pilling-Bedworth-ratio would be around 1.4 (above 1 there will be compressive stresses in the oxide scale), hence still in the good region between 1 and 2. For values below 1, there will be crack formation and for values above 2 there will be spallation of the oxide. Both multilayers (with $\Lambda = 130$ and 26 nm) exhibit similar oxide scale thicknesses (~ 700 nm) and morphologies composed of $\alpha\text{-Al}_2\text{O}_3$, $r\text{-TiO}_2$ as well Al_2TiO_5 , Fig. 5b.

4 Conclusions

The influence of the bilayer period and annealing in vacuum as well as ambient air on the spatially resolved in-plane strain/stress state of $\text{Ti}_{0.57}\text{Al}_{0.43}\text{N}/\text{Mo}_{0.58}\text{Si}_{0.28}\text{B}_{0.14}$ multilayers was studied in detail by position-resolved synchrotron X-ray nano-diffraction.

The $\text{Ti}_{0.57}\text{Al}_{0.43}\text{N}$ component is always single-phase fcc structured, regardless of the bilayer period ($\Lambda = 1085, 240, 130, \text{ and } 26$ nm) while the $\text{Mo}_{0.58}\text{Si}_{0.28}\text{B}_{0.14}$ layers are X-ray amorphous (in the as-deposited state). The competitive crystal growth of $\text{Ti}_{0.57}\text{Al}_{0.43}\text{N}$, which results in the typical V-shaped grains, is interrupted by the additional $\text{Mo}_{0.58}\text{Si}_{0.28}\text{B}_{0.14}$ layers, enforcing repeated renucleation of the $\text{Ti}_{0.57}\text{Al}_{0.43}\text{N}$ layers. Thereby, the development of a pronounced columnar structure is suppressed.

All as-deposited coatings show compressive residual strains with highest values directly at the interface to the substrate. But importantly, these significantly decrease with decreasing bilayer period, leading to a reduced loading at the substrate interface from -5.4 to -2.75 GPa when decreasing Λ from 1085 to 26 nm. During thermal loading of the multilayers to 900°C for 1 h (in vacuum as well as oxidising atmosphere), the formation of w-AlN (upon thermally induced decomposition of fcc- $\text{Ti}_{0.57}\text{Al}_{0.43}\text{N}$) is increasingly retarded with decreasing bilayer period. The combination of reduced interface loading and retarded formation of the spacious w-AlN allows that the multilayer with $\Lambda \leq 130$ nm still shows

an excellent adherence to the sapphire substrate even after the 1 h annealing treatment at 900 °C, whereas the other coatings experienced severe delamination.

The strain/stress profile of the multilayers (for the regions below the oxide scale) after 1 h oxidation at 900 °C is similar to that after vacuum annealing. Significantly smaller strains and stresses are present within the multilayer with the smallest bilayer period ($\Lambda = 26$ nm), because here the formation of spacious w-AlN is almost completely suppressed and mainly recovery effects are active. The oxide scale is with ~ 0.7 μm thickness comparable on both undelaminated multilayers (with $\Lambda = 130$ and 26 nm) and also the stress profile of the $r\text{-TiO}_2$ and $\alpha\text{-Al}_2\text{O}_3$ phases, which is slightly in the compressive state, is comparable.

The study clearly highlights the possibilities to influence the stress/strain state as well as related material properties such as hardness and indentation modulus by using architectural concepts, applicable in industrial manufacturing processes.

Acknowledgment

The financial support by the Austrian Federal Ministry of Economy, Family and Youth and the National Foundation for Research, Technology and Development is gratefully acknowledged. We also thank for the financial support of Plansee Composite Materials GmbH and Oerlikon Balzers, Oerlikon Surface Solutions AG. We acknowledge DESY (Hamburg, Germany), a member of the Helmholtz Association HGF, for the provision of experimental facilities. Parts of this research were carried out at PETRA III, at the Nanofocus Endstation of MINAXS (P03) beamline, equipped through financial support by the German Federal Ministry of Education and Research (BMBF projects 05KS7FK1 and 05K10FK3). TEM investigations were carried out using facilities of the USTEM centre of TU Wien, Austria

References

- [1] S. PalDey, S.C. Deevi, Single layer and multilayer wear resistant coatings of (Ti,Al)N: A review, *Mater Sci Eng A*. 342 (2003) 58–79. doi:10.1016/S0921-5093(02)00259-9.
- [2] K. Bobzin, High-performance coatings for cutting tools, *CIRP J Manuf Sci Technol*. 18 (2017) 1–9. doi:https://doi.org/10.1016/j.cirpj.2016.11.004.
- [3] P.H. Mayrhofer, L. Hultman, J.M. Schneiden, P. Staron, H. Clemens, Spinodal decomposition of cubic $\text{Ti}_{1-x}\text{Al}_x\text{N}$: Comparison between experiments and modeling, *Int J Mater Res*. 98 (2007) 1054–1059. doi:10.3139/146.101570.
- [4] P.H. Mayrhofer, D. Music, J.M. Schneider, Influence of the Al distribution on the structure, elastic properties, and phase stability of supersaturated $\text{Ti}_{1-x}\text{Al}_x\text{N}$, *J Appl Phys*. 100 (2006). doi:10.1063/1.2360778.
- [5] M. Bartosik, R. Daniel, Z. Zhang, M. Deluca, W. Ecker, M. Stefenelli, M. Klaus, C. Genzel, C.

- Mitterer, J. Keckes, Lateral gradients of phases, residual stress and hardness in a laser heated Ti 0.52Al 0.48N coating on hard metal, *Surf Coatings Technol.* 206 (2012) 4502–4510. doi:10.1016/j.surfcoat.2012.02.035.
- [6] L. Rogström, J. Ullbrand, J. Almer, L. Hultman, B. Jansson, M. Odén, Strain evolution during spinodal decomposition of TiAlN thin films, *Thin Solid Films.* 520 (2012) 5542–5549. doi:10.1016/j.tsf.2012.04.059.
- [7] M. Bartosik, C. Rumeau, R. Hahn, Z.L. Zhang, P.H. Mayrhofer, Fracture toughness and structural evolution in the TiAlN system upon annealing, *Sci Rep.* 7 (2017) 1–9. doi:10.1038/s41598-017-16751-1.
- [8] M. Bartosik, H.J. Böhm, C. Krywka, Z.L. Zhang, P.H. Mayrhofer, Influence of phase transformation on the damage tolerance of Ti-Al-N coatings, *Vacuum.* 155 (2018) 153–157. doi:10.1016/j.vacuum.2018.06.001.
- [9] L. Chen, Z.Q. Liu, Y.X. Xu, Y. Du, Influence of Zr on structure, mechanical and thermal properties of Cr-Al-N coatings, *Surf Coatings Technol.* 275 (2015) 289–295. doi:10.1016/j.surfcoat.2015.05.004.
- [10] W.J. Quadackers, V. Shemet, D. Sebold, R. Anton, E. Wessel, L. Singheiser, Oxidation characteristics of a platinized MCrAlY bond coat for TBC systems during cyclic oxidation at 1000 °C, *Surf Coatings Technol.* 199 (2005) 77–82. doi:10.1016/j.surfcoat.2004.11.038.
- [11] R. Hollerweger, H. Riedl, J. Paulitsch, M. Arndt, R. Rachbauer, P. Polcik, S. Primig, P.H. Mayrhofer, Origin of high temperature oxidation resistance of Ti-Al-Ta-N coatings, *Surf Coatings Technol.* 257 (2014) 78–86. doi:10.1016/j.surfcoat.2014.02.067.
- [12] J. Todt, R. Pitonak, A. Köpf, R. Weißenbacher, B. Sartory, M. Burghammer, R. Daniel, T. Schöberl, J. Keckes, Superior oxidation resistance, mechanical properties and residual stresses of an Al-rich nanolamellar Ti_{0.05}Al_{0.95}N coating prepared by CVD, *Surf Coatings Technol.* 258 (2014) 1119–1127. doi:10.1016/j.surfcoat.2014.07.022.
- [13] J. Keckes, M. Bartosik, R. Daniel, C. Mitterer, G. Maier, W. Ecker, C. David, S. Schoeder, M. Burghammer, X-ray nanodiffraction reveals strain and microstructure evolution in nanocrystalline thin films, *Scr Mater.* 67 (2012) 748–751. doi:10.1016/j.scriptamat.2012.07.034.
- [14] R. Daniel, J. Keckes, I. Matko, M. Burghammer, C. Mitterer, Origins of microstructure and stress gradients in nanocrystalline thin films : The role of growth parameters and self-organization, *Acta Mater.* 61 (2013) 6255–6266. doi:10.1016/j.actamat.2013.07.009.
- [15] R. Hammer, J. Todt, J. Keckes, B. Sartory, G. Parteder, J. Kraft, S. Defregger, High resolution residual stress gradient characterization in W/TiN-stack on Si (100): Correlating in-plane stress and grain size distributions in W sublayer, *Mater Des.* 132 (2017) 72–78.

doi:10.1016/j.matdes.2017.06.052.

- 420 [16] J. Keckes, R. Daniel, J. Todt, J. Zalesak, B. Sartory, S. Braun, J. Gluch, M. Rosenthal, M. Burghammer, C. Mitterer, S. Niese, A. Kubec, 30 nm X-ray focusing correlates oscillatory stress , texture and structural defect gradients across multilayered TiN-SiO_x thin film, *Acta Mater.* 144 (2018) 862–873. doi:10.1016/j.actamat.2017.11.049.
- [17] M. Bartosik, J. Keckes, P.O.Å. Persson, H. Riedl, P.H. Mayrhofer, Interface controlled microstructure evolution in nanolayered thin films, *SMM.* 123 (2016) 13–16. doi:10.1016/j.scriptamat.2016.05.031.
- [18] E. Aschauer, S. Sackl, T. Schachinger, T. Wojcik, M. Arndt, P. Polcik, H. Riedl, P.H. Mayrhofer, Nano-structural investigation of Ti-Al-N/Mo-Si-B multilayer coatings: A comparative study between APT and HR-TEM, *Vaccum.* 157 (2018) 173–179.
- [19] H. Riedl, E. Aschauer, C.M. Koller, P. Polcik, M. Arndt, P.H. Mayrhofer, Ti-Al-N/Mo-Si-B multilayers: An architectural arrangement for high temperature oxidation resistant hard coatings, *Surf Coat Technol.* 328 (2017) 80–88. doi:10.1016/j.surfcoat.2017.08.032.
- 430 [20] E. Aschauer, S. Sackl, T. Schachinger, H. Bolvardi, M. Arndt, P. Polcik, H. Riedl, P.H. Mayrhofer, Atomic scale investigations of thermally treated nano-structured Ti-Al-N/Mo-Si-B multilayers, *Surf Coat Technol.* 349 (2018) 480–487. doi:10.1016/j.surfcoat.2018.06.026.
- [21] F. Wang, I.A. Abrikosov, S.I. Simak, M. Odén, F. Mücklich, F. Tasnádi, Coherency effects on the mixing thermodynamics of cubic Ti_{1-x}Al_xN/TiN (001) multilayers, *Phys Rev B.* 93 (2016) 1–7. doi:10.1103/PhysRevB.93.174201.
- [22] E. Vogli, W. Tillmann, U. Selvadurai-Iassl, G. Fischer, J. Herper, Influence of Ti/TiAlN-multilayer designs on their residual stresses and mechanical properties, *Appl Surf Sci.* 257 (2011) 8550–8557. doi:10.1016/j.apsusc.2011.05.013.
- [23] C. Krywka, J. Keckes, S. Storm, A. Buffet, S.V. Roth, R. Döhrmann, M. Müller, Nanodiffraction at MINAXS (P03) beamline of, *J Phys Conf Ser.* (2013) 8–12. doi:10.1088/1742-6596/425/7/072021.
- 440 [24] M. Bartosik, R. Daniel, C. Mitterer, I. Matko, M. Burghammer, P.H. Mayrhofer, J. Keckes, Cross-sectional X-ray nanobeam diffraction analysis of a compositionally graded CrN_x thin film, 542 (2013) 1–4. doi:10.1016/j.tsf.2013.05.102.
- [25] A.P. Hammersley, S.O. Svensson, M. Hanfland, A.N. Fitch, D. Hausermann, Two-dimensional detector software: From real detector to idealised image or two-theta scan, *High Press Res.* 14 (1996) 235–248. doi:10.1080/08957959608201408.
- [26] M. Stefanelli, R. Daniel, W. Ecker, D. Kiener, J. Todt, A. Zeilinger, C. Mitterer, M. Burghammer, X-ray nanodiffraction reveals stress distribution across an indented multilayered CrN – Cr thin film, *Acta Mater.* 85 (2015) 24–31. doi:10.1016/j.actamat.2014.11.011.

[27] P. Ström, P. Petersson, M. Rubel, G. Possnert, A combined segmented anode gas ionization chamber and time-of-flight detector for heavy ion elastic recoil detection analysis, *Rev Sci Instrum.* 87 (2016) 103303. doi:10.1063/1.4963709.

[28] A. Anders, A structure zone diagram including plasma-based deposition and ion etching, *Thin Solid Films.* 518 (2010) 4087–4090. doi:10.1016/j.tsf.2009.10.145.

[29] J.E. Daalder, Erosion and the origin of charged and neutral species in vacuum arcs Erosion and the origin of charged and neutral species in vacuum arcs, *J Appl Phys.* 8 (1975) 1647.

[30] C.M. Koller, J. Ramm, S. Kolozsvári, J. Paulitsch, P.H. Mayrhofer, Role of droplets and iron on the phase formation of arc evaporated Al – Cr-oxide coatings, *Surf Coat Technol.* 276 (2015) 735–742. doi:10.1016/j.surfcoat.2015.05.012.

[31] F. Döhler, S. Kasch, T. Schmidt, C. Rüssel, Sealing of alumina using a CO₂ laser and a rapidly crystallizing glass, *J Mater Process Tech.* 233 (2016) 206–211. doi:10.1016/j.jmatprotec.2016.02.020.

[32] S. PalDey, S.C. Deevi, Single layer and multilayer wear resistant coatings of (Ti,Al)N: A review, *Mater Sci Eng A.* 342 (2003) 58–79.

[33] M. Bartosik, D. Holec, D. Apel, M. Klaus, C. Genzel, J. Keckes, M. Arndt, P. Polcik, C.M. Koller, P.H. Mayrhofer, Thermal expansion of Ti-Al-N and Cr-Al-N coatings, *Scr Mater.* 127 (2017) 182–185. doi:10.1016/j.scriptamat.2016.09.022.

[34] W.M. Seidl, M. Bartosik, S. Kolozsvári, H. Bolvardi, P.H. Mayrhofer, Influence of coating thickness and substrate on stresses and mechanical properties of (Ti,Al,Ta)N/(Al,Cr)N multilayers, *Surf Coat Technol.* 347 (2018) 92–98. doi:10.1016/j.surfcoat.2018.04.060.

[35] H. Ljungcrantz, C. Engström, L. Hultman, M. Olsson, X. Chu, M.S. Wong, W.D. Sproul, polycrystalline nanostructured multilayer films grown by reactive magnetron sputtering Nanoindentation hardness , abrasive wear , and microstructure of TiN/NbN polycrystalline nanostructured multilayer films grown by reactive magnetron sputtering, *J Vac Sci Technol A.* 3104 (2010). doi:10.1116/1.581466.

[36] R. Rachbauer, S. Massl, E. Stergar, D. Holec, D. Kiener, J. Keckes, J. Patscheider, M. Stiefel, H. Leitner, H. Mayrhofer, Decomposition pathways in age hardening of Ti-Al-N films, *J Appl Phys.* 110 (2011) 23515. doi:10.1063/1.3610451.